

Directional reflection modeling via wavenumber-domain reflection coefficient for 3D acoustic field simulation

Satoshi Hoshika and Takahiro Iwami

Graduate School of Design, Kyushu University, Fukuoka, Japan
hoshikasatoshi@gmail.com, iwami@design.kyushu-u.ac.jp

Akira Omoto

Faculty of Design, Kyushu University, Fukuoka, Japan
omoto@design.kyushu-u.ac.jp

Abstract

This study proposes a framework for incorporating wavenumber-domain acoustic reflection coefficients into sound field analysis to characterize direction-dependent material reflection and scattering phenomena. The reflection coefficient is defined as the amplitude ratio between incident and reflected waves for each propagation direction and is estimated from spatial Fourier transforms of the incident and reflected sound fields. The resulting wavenumber-domain reflection coefficients are converted into an acoustic admittance representation that is directly compatible with numerical methods such as the Boundary Element Method (BEM), enabling simulation of reflections beyond simple specular components. Unlike conventional extended reaction models, the proposed approach avoids explicit modeling of the material interior. This significantly reduces computational cost while allowing direct use of measured data, empirical models, or user-defined directional reflection characteristics. The validity of the proposed formulation was previously demonstrated by the authors through two-dimensional sound field simulations, in which accurate reproduction of direction-dependent reflection behavior was confirmed. In the present work, the framework is extended to three-dimensional analysis, demonstrating its applicability to more realistic and complex acoustic environments. The proposed approach provides a practical and flexible tool for simulating direction-dependent acoustic reflections and scattering, with potential applications in architectural acoustics, material characterization, and noise control.

Submitted to Proceedings of Meetings on Acoustics (PoMA 2025).

1 Background and Motivation

Impedance boundary conditions have long been used as a standard approach for modeling sound absorption and reflection at material surfaces. In their simplest form, such boundary conditions relate the normal particle velocity to the sound pressure at the surface and provide an efficient means of representing energy dissipation without explicitly resolving the interior of the material. However, locally reactive impedance models inherently neglect directional effects and are unable to describe non-specular reflection or scattering phenomena.

To address these limitations, extended reaction models have been developed to account for wave propagation and energy dissipation within the material interior. Representative examples include equivalent fluid models [1, 2], Biot-type poroelastic models [3, 4], and numerical analyses of periodic or layered structures [5, 6]. While these approaches enable the prediction of angle-dependent reflection and scattering characteristics, they require volumetric discretization of the material domain. In three-dimensional simulations, this

leads to a substantial increase in computational cost, often resulting in meshes consisting of several tens or hundreds of thousands of elements. Furthermore, resolving directional reflection behavior typically requires multiple simulations for different incident angles, which further compounds the computational burden.

In contrast to these approaches, the present study adopts a macroscopic viewpoint that focuses exclusively on the relationship between incident and reflected waves at the boundary. Rather than modeling the internal dynamics of the material, the proposed framework treats the boundary as a linear operator that redistributes incident acoustic energy among reflected directions. This relationship is described in terms of propagation directions by applying a spatial Fourier transform to the boundary pressure field, which enables the incident and reflected sound fields to be decomposed into plane-wave components indexed by in-plane wavenumbers. This perspective is particularly suited to applications where the internal microstructure is unknown, too complex to model explicitly, or unnecessary for describing the observable reflection behavior.

Spatial Fourier transform techniques have previously been employed to analyze directional reflection characteristics at boundaries. For example, Tamura proposed a method to estimate angle-dependent reflection coefficients from measured sound pressure distributions using a spatial Fourier transform [7, 8]. Although this approach enables the evaluation of oblique incidence effects, the reflection coefficient is treated as a scalar quantity defined independently for each incident direction. As a result, non-specular reflection and directional coupling between different wave components cannot be represented within a unified framework.

To overcome this limitation, the authors previously introduced the concept of a *wavenumber-domain acoustic reflection coefficient*, denoted by \mathbf{C}_r , which represents a linear mapping between incident and reflected wave components in wavenumber space [9, 10]. This operator-based formulation naturally captures non-specular reflection and multi-directional scattering without invoking volumetric models of the material interior. However, previous studies were primarily limited to two-dimensional sound fields, and a systematic extension to three-dimensional problems, as well as a practical integration of the estimated reflection characteristics into numerical sound field simulations, had not yet been established.

The objective of the present study is to construct a unified framework for describing directional acoustic reflection in three-dimensional sound fields. The proposed method estimates the wavenumber-domain reflection matrix \mathbf{C}_r from spatial distributions of incident and reflected waves obtained using multiple sound sources and receivers. The estimated matrix is then transformed into a wavenumber-domain admittance and incorporated into a conventional boundary element method (BEM) as a non-local boundary condition. This enables complex angle-dependent reflection and scattering behavior to be reproduced directly at the boundary, while avoiding the high computational cost associated with extended reaction models that explicitly resolve the material interior.

2 Principle of the Wavenumber-Domain Reflection Coefficient Estimation in 3D Field

2.1 Definition of the Wavenumber-Domain Acoustic Reflection Coefficient

We consider an incident and a reflected acoustic wave in a three-dimensional acoustic field, as illustrated in Fig. 1. The material surface is located at $\Gamma = \{ \mathbf{r} = (x, y, z) \in \mathbb{R}^3 \mid z = 0 \}$, and the incident and reflected sound pressures are denoted by p_i and p_r , respectively. All quantities are treated in the frequency domain, and the angular frequency ω is omitted for brevity.

We regard the pressure distribution on the boundary plane and its Fourier transform as finite-energy signals and adopt the Hilbert space $L^2(\mathbb{R}^2)$ as the functional setting. In wavenumber-domain analysis, only

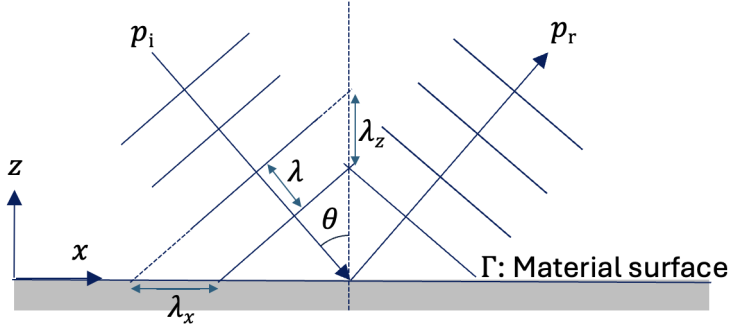


Figure 1: Schematic illustration of reflection in a three-dimensional acoustic field. A plane wave is incident from the upper half-space onto the boundary surface at $z = 0$, where it is reflected back into the same half-space.

the components parallel to the boundary, (k_x, k_y) , are considered:

$$\mathbf{k}_{xy} := (k_x, k_y), \quad \mathcal{D}_k := \{ \mathbf{k}_{xy} \in \mathbb{R}^2 \mid k_x^2 + k_y^2 \leq k^2 \}.$$

Evanescence components satisfying $|\mathbf{k}_{xy}| > k$ do not contribute to the radiated far field and are therefore neglected.

The two-dimensional Fourier transform along the boundary plane is defined as [11]

$$\mathcal{F}_{xy} f(\mathbf{k}_{xy}) := \frac{1}{2\pi} \iint_{\mathbb{R}^2} f(x, y) e^{-i(k_x x + k_y y)} dx dy, \quad (1)$$

$$\mathcal{F}_{xy}^{-1} \hat{f}(x, y) := \frac{1}{2\pi} \iint_{\mathbb{R}^2} \hat{f}(\mathbf{k}_{xy}) e^{i(k_x x + k_y y)} dk_x dk_y. \quad (2)$$

Representing the three-dimensional wavenumber vector in spherical coordinates,

$$k_x = k \sin \theta \cos \phi, \quad k_y = k \sin \theta \sin \phi, \quad k_z = k \cos \theta, \quad (3)$$

where for propagating components $|k_z| = \sqrt{k^2 - k_x^2 - k_y^2}$.

Using this representation, the incident and reflected wavenumber-domain spectra are defined on the same domain \mathcal{D}_k but are distinguished by the sign of the normal wavenumber component:

$$\hat{p}_i(\mathbf{k}_{xy}) := \mathcal{F}_{xy} p_i(\mathbf{k}_{xy}), \quad k_z < 0, \quad (4)$$

$$\hat{p}_r(\mathbf{k}_{xy}) := \mathcal{F}_{xy} p_r(\mathbf{k}_{xy}), \quad k_z > 0. \quad (5)$$

That is, \hat{p}_i represents plane-wave components propagating toward the boundary, whereas \hat{p}_r corresponds to components propagating away from the boundary after reflection.

The incident and reflected fields can then be expressed by plane-wave expansions as

$$p_i(x, y, z) = \frac{1}{2\pi} \iint_{\mathcal{D}_k} \hat{p}_i(\mathbf{k}_{xy}) e^{i(k_x x + k_y y - |k_z|z)} d\mathbf{k}_{xy}, \quad (6)$$

$$p_r(x, y, z) = \frac{1}{2\pi} \iint_{\mathcal{D}_k} \hat{p}_r(\mathbf{k}_{xy}) e^{i(k_x x + k_y y + |k_z|z)} d\mathbf{k}_{xy}. \quad (7)$$

Using the boundary-plane spectra, the reflection operator can be written as

$$\hat{p}_r(\mathbf{k}_{xy}) = \iint_{\mathcal{D}_k} C_r(\mathbf{k}_{xy}, \mathbf{k}'_{xy}) \hat{p}_i(\mathbf{k}'_{xy}) d\mathbf{k}'_{xy}, \quad (8)$$

where the reflection operator $\mathcal{C}_r : L^2(\mathcal{D}_k) \rightarrow L^2(\mathcal{D}_k)$ is defined as

$$\mathcal{C}_r \hat{f}(\mathbf{k}_{xy}) := \iint_{\mathcal{D}_k} C_r(\mathbf{k}_{xy}, \mathbf{k}'_{xy}) \hat{f}(\mathbf{k}'_{xy}) d\mathbf{k}'_{xy}.$$

Considering energy balance and dissipation, the operator norm satisfies $\|\mathcal{C}_r\|_{\text{op}} \leq 1$, and strictly $\|\mathcal{C}_r\|_{\text{op}} < 1$ unless the boundary is perfectly reflecting [12].

For numerical implementation, the wavenumber domain \mathcal{D}_k is discretized by sampling points $\{\mathbf{k}_{xy,m}\}_{m=1}^M$ with associated quadrature weights $w_m > 0$, which represent the integration measure corresponding to the finite area in the wavenumber plane covered by each discrete mode. Accordingly, the continuous integral is approximated as

$$\iint_{\mathcal{D}_k} f(\mathbf{k}_{xy}) d\mathbf{k}_{xy} \approx \sum_{n=1}^M f(\mathbf{k}_{xy,n}) w_n.$$

The reflected spectrum is thus discretized as

$$\hat{p}_r(\mathbf{k}_{xy,m}) \approx \sum_{n=1}^M C_r(\mathbf{k}_{xy,m}, \mathbf{k}_{xy,n}) \hat{p}_i(\mathbf{k}_{xy,n}) w_n.$$

The specific form of w_n depends on the sampling scheme used to discretize \mathcal{D}_k . For example, when a Fibonacci lattice is employed to uniformly sample the upper hemisphere, the quadrature weight can be approximated as

$$w_n \approx \frac{2\pi k k_{z,n}}{M},$$

where k is the acoustic wavenumber, $k_{z,n}$ is the normal component of the n -th wavenumber vector, and M is the total number of sampled modes. This choice ensures an approximately uniform partition of solid angle and energy-consistent discretization of the reflection operator.

Define the vectors

$$\hat{\mathbf{p}}_i = [\hat{p}_i(\mathbf{k}_{xy,1}), \dots, \hat{p}_i(\mathbf{k}_{xy,M})]^T, \quad (9)$$

$$\hat{\mathbf{p}}_r = [\hat{p}_r(\mathbf{k}_{xy,1}), \dots, \hat{p}_r(\mathbf{k}_{xy,M})]^T. \quad (10)$$

Defining the matrix

$$[\mathbf{C}_r]_{mn} := C_r(\mathbf{k}_{xy,m}, \mathbf{k}_{xy,n}) w_n,$$

the discrete relation can be written as

$$\hat{\mathbf{p}}_r = \mathbf{C}_r \hat{\mathbf{p}}_i. \quad (11)$$

Diagonal elements of \mathbf{C}_r correspond to specular reflection, whereas off-diagonal elements represent scattering-induced directional coupling.

2.2 Estimation of the Wavenumber-Domain Reflection Coefficient (3D)

Based on Eq. (11), the wavenumber-domain reflection matrix \mathbf{C}_r is estimated from Q sets of incident and reflected spectra. Stacking these spectra column-wise yields

$$\hat{\mathcal{P}}_i = [\hat{\mathbf{p}}_{i,1}, \dots, \hat{\mathbf{p}}_{i,Q}] \in \mathbb{C}^{M \times Q}, \quad (12)$$

$$\hat{\mathcal{P}}_r = [\hat{\mathbf{p}}_{r,1}, \dots, \hat{\mathbf{p}}_{r,Q}] \in \mathbb{C}^{M \times Q}. \quad (13)$$

These matrices satisfy the linear relation

$$\hat{\mathcal{P}}_r = \mathbf{C}_r \hat{\mathcal{P}}_i, \quad (14)$$

from which \mathbf{C}_r can be estimated, for example, using the Moore–Penrose pseudoinverse as

$$\mathbf{C}_r \simeq \hat{\mathcal{P}}_r \hat{\mathcal{P}}_i^\dagger, \quad (15)$$

where $(\cdot)^\dagger$ denotes the pseudoinverse.

For boundaries with homogeneous or periodic structure, the reflected wavefield often concentrates into a limited number of wavenumber components. As a result, the corresponding reflection matrix \mathbf{C}_r tends to exhibit a sparse or approximately sparse structure in wavenumber space. When such structure is anticipated, sparsity-promoting estimation techniques, such as ℓ_1 -regularized regression, can be employed as an alternative solution strategy to enhance robustness under limited or noisy observations. In the present study, this type of regularization is used as a practical option, while the proposed framework itself is not restricted to any specific estimation method.

3 Admittance Operator and Its Application to Numerical Simulations

3.1 Derivation of the Normalized Acoustic Admittance Operator and Its Matrix Representation

As shown in the previous section, the reflection coefficient in the wavenumber domain describes how an incident wave is reflected at a boundary in terms of both direction and amplitude. In this section, we present a framework for applying this theory to numerical simulations by transforming the reflection coefficient into a normalized acoustic admittance. This formulation is particularly useful for numerical methods in which boundary conditions are expressed in terms of admittance, such as the boundary element method (BEM). To this end, the admittance operator is derived from the relationship between sound pressure and particle velocity in the wavenumber domain.

We define the normalized acoustic admittance operator $(\mathcal{B} : L^2(\mathcal{D}_k) \rightarrow L^2(\mathcal{D}_k))$, which maps sound pressure to particle velocity in the wavenumber domain, as

$$\mathcal{B} \hat{p}(\mathbf{k}_{xy}) = \hat{v}(\mathbf{k}_{xy}). \quad (16)$$

The sound pressure field in the wavenumber domain, $\hat{p}(\mathbf{k}_{xy}, z)$, can be expressed as the superposition of the incident and reflected waves as

$$\hat{p}(\mathbf{k}_{xy}, z) = \hat{p}_i(\mathbf{k}_{xy}) e^{-ik_z z} + \hat{p}_r(\mathbf{k}_{xy}) e^{ik_z z}. \quad (17)$$

Let ρ and c denote the density and sound speed of the medium, respectively. The particle velocity in the z -direction, $\hat{v}(\mathbf{k}_{xy}, z)$, is obtained from Euler's equation as

$$\hat{v}(\mathbf{k}_{xy}, z) = \frac{1}{i\rho\omega} \frac{\partial}{\partial z} \hat{p}(\mathbf{k}_{xy}, z) = \frac{k_z}{\rho c k} \left(-\hat{p}_i(\mathbf{k}_{xy}) e^{-ik_z z} + \hat{p}_r(\mathbf{k}_{xy}) e^{ik_z z} \right). \quad (18)$$

At the boundary $z = 0$, the sound pressure and particle velocity are given by

$$\hat{p}(\mathbf{k}_{xy}) = \hat{p}_i(\mathbf{k}_{xy}) + \hat{p}_r(\mathbf{k}_{xy}), \quad (19)$$

$$\hat{v}(\mathbf{k}_{xy}) = \frac{k_z}{\rho c k} (-\hat{p}_i(\mathbf{k}_{xy}) + \hat{p}_r(\mathbf{k}_{xy})). \quad (20)$$

Using the reflection coefficient operator \mathcal{C}_r and the identity operator \mathcal{I} , the pressure and particle velocity can be rewritten as

$$\hat{p}(\mathbf{k}_{xy}) = (\mathcal{I} + \mathcal{C}_r) \hat{p}_i(\mathbf{k}_{xy}), \quad (21)$$

$$\hat{v}(\mathbf{k}_{xy}) = \hat{\beta}_0(\mathbf{k}_{xy}) (-\mathcal{I} + \mathcal{C}_r) \hat{p}_i(\mathbf{k}_{xy}), \quad (22)$$

where $\hat{\beta}_0(\mathbf{k}_{xy})$ denotes the characteristic admittance corresponding to the in-plane wavenumber \mathbf{k}_{xy} , defined as

$$\hat{\beta}_0(\mathbf{k}_{xy}) := \frac{k_z}{\rho c k} = \frac{\sqrt{k^2 - (k_x^2 + k_y^2)}}{\rho c k}. \quad (23)$$

This quantity is equal to $\hat{\beta}_0(\mathbf{k}_{xy}) = \cos \theta / (\rho c)$, where θ is the angle of incidence, and represents the characteristic admittance for obliquely incident waves [13].

Substituting Eqs. (21) and (22) into Eq. (16), we obtain

$$\mathcal{B}(\mathcal{I} + \mathcal{C}_r) \hat{p}_i(\mathbf{k}_{xy}) = \hat{\beta}_0(\mathbf{k}_{xy}) (-\mathcal{I} + \mathcal{C}_r) \hat{p}_i(\mathbf{k}_{xy}). \quad (24)$$

To construct the normalized acoustic admittance operator \mathcal{B} using $(\mathcal{I} + \mathcal{C}_r)^{-1}$, the invertibility of $(\mathcal{I} + \mathcal{C}_r)$ is required. This invertibility is guaranteed by the Neumann series expansion in operator theory. As discussed in the previous section, \mathcal{C}_r is a bounded linear integral operator on $L^2(\mathcal{D}_k)$, and its operator norm satisfies $\|\mathcal{C}_r\|_{\text{op}} < 1$ due to energy conservation and the presence of small dissipation. Therefore,

$$(\mathcal{I} + \mathcal{C}_r)^{-1} = \sum_{n=0}^{\infty} (-\mathcal{C}_r)^n,$$

and invertibility is ensured by norm convergence.

Consequently, the normalized acoustic admittance operator \mathcal{B} is given by

$$\mathcal{B} = \hat{\beta}_0(\mathbf{k}_{xy}) (-\mathcal{I} + \mathcal{C}_r) (\mathcal{I} + \mathcal{C}_r)^{-1}. \quad (25)$$

In numerical computations, the continuous wavenumber space is approximated by a finite-dimensional representation. By discretizing the wavenumber plane \mathcal{D}_k into a finite set of points $\{\mathbf{k}_{xy,1}, \mathbf{k}_{xy,2}, \dots, \mathbf{k}_{xy,M}\}$, the matrix representation of the normalized acoustic admittance based on Eq. (25) is obtained as

$$\mathbf{B} = \mathbf{B}_0 (-\mathbf{I} + \mathbf{C}_r) (\mathbf{I} + \mathbf{C}_r)^{-1}, \quad (26)$$

where $\mathbf{I} \in \mathbb{R}^{M \times M}$ is the identity matrix and $\mathbf{B}_0 \in \mathbb{R}^{M \times M}$ is a diagonal matrix whose elements correspond to the characteristic admittance of the medium, defined as

$$\mathbf{B}_0 := \text{diag} \left(\frac{\sqrt{k^2 - (k_{x,1}^2 + k_{y,1}^2)}}{\rho c k}, \frac{\sqrt{k^2 - (k_{x,2}^2 + k_{y,2}^2)}}{\rho c k}, \dots, \frac{\sqrt{k^2 - (k_{x,M}^2 + k_{y,M}^2)}}{\rho c k} \right).$$

Accordingly, for a pressure vector in the wavenumber domain $\hat{\mathbf{p}} \in \mathbb{C}^M$, the corresponding particle velocity vector $\hat{\mathbf{v}} \in \mathbb{C}^M$ is computed as

$$\hat{\mathbf{v}} = \mathbf{B} \hat{\mathbf{p}}.$$

3.2 Application of Wavenumber-Domain Admittance to the Boundary Element Method

The Boundary Element Method (BEM) evaluates sound pressure and particle velocity on a boundary by discretizing the boundary integral equation derived from the Kirchhoff–Helmholtz integral theorem, and is widely used for acoustic absorption and scattering analyses [14, 15].

Consider a domain Ω containing a point source of strength A located at \mathbf{r}_s . The sound pressure field $p(\mathbf{r})$ satisfies the Kirchhoff–Helmholtz integral equation, where G denotes the free-field Green's function, k the acoustic wavenumber, and ρ the medium density. For observation points on the boundary Γ , the solid-angle coefficient is $\epsilon = 1/2$. After discretizing Γ into N_b boundary elements, the standard BEM formulation can be written in matrix form as

$$\frac{1}{2} \mathbf{p} = A \mathbf{g}_s + \mathbf{G}' \mathbf{p} - i\omega\rho \mathbf{G} \mathbf{v}, \quad (27)$$

where \mathbf{p} and \mathbf{v} denote the boundary pressure and particle velocity vectors, respectively.

Conventional BEM assumes a locally reactive boundary by imposing a pointwise relation $\mathbf{v} = \beta \mathbf{p}$. While this approximation is valid for normal incidence, it fails to capture direction-dependent behavior at oblique incidence. To overcome this limitation, the present study introduces a nonlocal boundary operator defined in the wavenumber domain.

Applying a spatial Fourier transform to the boundary pressure distribution, the particle velocity on the boundary can be expressed in operator form as

$$\mathbf{v} = \tilde{\mathbf{F}}_{xy}^H \mathbf{W}_k \mathbf{B} \tilde{\mathbf{F}}_{xy} \mathbf{p} = \hat{\mathbf{B}} \mathbf{p}, \quad (28)$$

where $\mathbf{B} \in \mathbb{C}^{n_k \times n_k}$ denotes the specific acoustic admittance matrix in the wavenumber domain and $\hat{\mathbf{B}}$ its spatial-domain counterpart. The matrix $\tilde{\mathbf{F}}_{xy} \in \mathbb{C}^{n_k \times N_b}$ represents the whitened spatial Fourier transform defined below. Substituting Eq. (28) into Eq. (27) yields a closed BEM system that can be solved using standard linear solvers.

The spatial Fourier transform matrix \mathbf{F}_{xy} is constructed as a discrete approximation of the continuous two-dimensional Fourier transform defined in Eq. (1). Using N_b boundary element centers $\{(x_m, y_m)\}_{m=1}^{N_b}$ on the plane $z = 0$ and n_k discrete in-plane wavenumber vectors $\{\mathbf{k}_{xy,i}\}_{i=1}^{n_k}$, its elements are defined as

$$[\mathbf{F}_{xy}]_{im} = \frac{1}{2\pi} \exp(-i \mathbf{k}_{xy,i} \cdot \mathbf{r}_{xy,m}), \quad (29)$$

where $\mathbf{r}_{xy,m} = (x_m, y_m)$. The factor $1/(2\pi)$ follows directly from the continuous Fourier transform convention, whereas the discretization of the integration measure is handled separately through the quadrature weights introduced in Subsection 2.1.

Because the wavenumber domain \mathcal{D}_k is discretized, the resulting set of plane-wave basis functions is not exactly orthogonal under the continuous energy inner product, and in general $\mathbf{F}_{xy}^H \mathbf{W}_k \mathbf{F}_{xy} \neq \mathbf{I}$.

To compensate for this numerical non-orthogonality, a whitening normalization is applied based on the weighted Gram matrix

$$\mathbf{H} = \mathbf{F}_{xy}^H \mathbf{W}_k \mathbf{F}_{xy}.$$

The inverse square root $\mathbf{H}^{-1/2}$ is defined as the Hermitian positive-definite matrix satisfying $\mathbf{H}^{-1/2} \mathbf{H} \mathbf{H}^{-1/2} = \mathbf{I}$, and can be computed, for example, via an eigenvalue decomposition of \mathbf{H} .

Using this definition, the normalized spatial Fourier transform matrix is given by

$$\tilde{\mathbf{F}}_{xy} = \mathbf{F}_{xy} \mathbf{H}^{-1/2}, \quad (30)$$

which satisfies the weighted orthonormality condition $\tilde{\mathbf{F}}_{xy}^H \mathbf{W}_k \tilde{\mathbf{F}}_{xy} = \mathbf{I}$. Employing $\tilde{\mathbf{F}}_{xy}$ in Eq. (28) eliminates artificial coupling between plane-wave components and enables stable boundary element simulations with direction-dependent boundary operators beyond locally reactive models.

4 Numerical Experiment I: Estimation of the Wavenumber-Domain Reflection Coefficient

4.1 Simulation Conditions

To validate the effectiveness of the proposed wavenumber-domain reflection coefficient estimation method, a numerical simulation was carried out. Two types of boundaries were considered: a flat plate exhibiting specular reflection and a periodic slit structure producing multi-directional scattering. Both boundaries were modeled as acoustically rigid surfaces (Neumann condition).

The sound sources were positioned 0.1 m above the reflecting surface, and 100 omnidirectional point sources were distributed around this height. The source height and radial distance ($r = 0.75$ m) were fixed, and the spatial distribution was determined using Fibonacci sampling to avoid directional bias. Receiver points were placed 0.01 m above the reflecting surface, arranged in a regular grid of 400 points with a spacing of 0.04 m. The source-receiver configuration is illustrated in Figs. 2a (flat plate) and 2b (slit).

Each source was sequentially excited, and the incident and reflected wavefields were computed using frequency-domain BEM. The resulting multi-source/multi-receiver pressure dataset was processed using ℓ_1 -regularized solver (LASSO[16]) as a practical option to estimate the reflection coefficient matrix \mathbf{C}_r , representing the directional mapping between incident and reflected wave components in the wavenumber domain.

The slit boundary consisted of rigid bars with a width of 0.05 m arranged periodically with a pitch of 0.10 m. The same source and receiver configuration was used for both boundary conditions to enable a direct comparison.

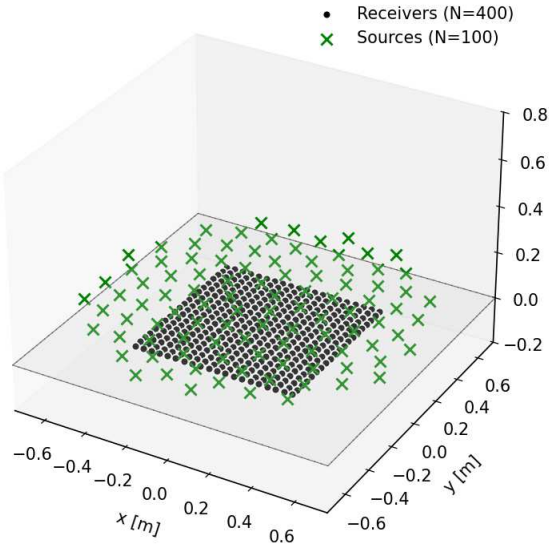
The excitation frequency was set to 3.4 kHz, such that the acoustic wavelength is on the same order as the characteristic length scale of the slit geometry. This choice allows diffraction and multi-directional scattering effects induced by the periodic structure to be clearly manifested, while remaining within a frequency range that can be accurately resolved by the numerical discretization.

The speed of sound was set to $c = 343.5$ m/s and the air density to $\rho = 1.205$ kg/m³.

4.2 Results

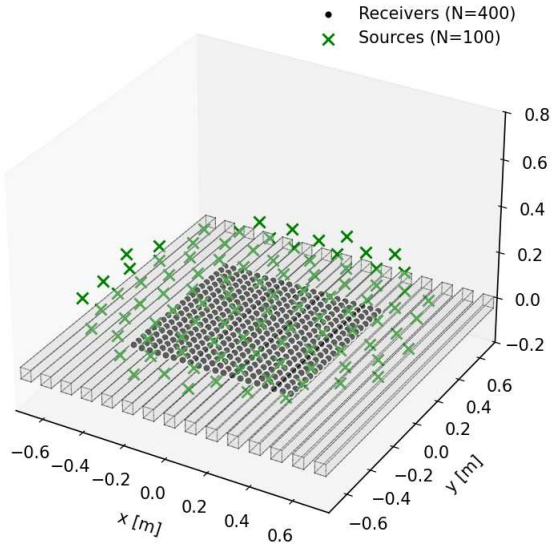
Figures 3(a) and 3(b) show the estimated wavenumber-domain reflection coefficient matrices \mathbf{C}_r for the flat plate and periodic slit boundaries, respectively. The horizontal axis represents the incident wavenumber

Measurement layout (Fibonacci spiral sources)



(a) Flat plate boundary condition

Measurement layout (Fibonacci spiral sources)



(b) Periodic slit boundary condition

Figure 2: Numerical analysis setup for the two boundary conditions (units in meters). Omnidirectional point sources (white triangles) are placed on a plane 0.10 m above the boundary surface. A total of 100 sources are distributed with a fixed radial distance of $r = 0.75$ m using Fibonacci sampling to ensure an approximately uniform angular distribution without directional bias. Receiver points (white circles) are located on a plane 0.01 m above the boundary and arranged in a regular grid of 400 points with a spacing of 0.04 m. (a) Flat plate boundary condition; (b) Periodic slit boundary condition. Both boundaries are modeled as acoustically rigid (Neumann) surfaces.

ber mode index, and the vertical axis represents the reflected mode index. For visual clarity, the number of wavenumber bins was set to 400. For the flat-plate condition shown in Fig. 3(a), the matrix energy is strongly concentrated along the main diagonal, confirming the dominance of specular reflection as theoretically expected. In contrast, the periodic slit condition shown in Fig. 3(b) exhibits pronounced off-diagonal components, clearly capturing the multi-directional scattering induced by the periodic structure.

To examine the validity of the estimated \mathbf{C}_r , reflection directivity maps $|P_r|$ were reconstructed using the matrices. Figure 4(a) presents the reflected pressure distributions for the flat plate, while Fig. 4(b) shows the corresponding results for the periodic slit, under incident angles $\theta_i = 0^\circ, 30^\circ$, and 60° . The blue cross marks indicate the incident direction, enabling intuitive visualization of how acoustic energy is redistributed into specular and scattered directions. The incident-wave vector $\hat{\mathbf{p}}_i$ used for the reconstruction was defined as a one-hot vector, in which only the component corresponding to the incident direction was set to unity. This formulation allows direct evaluation of how accurately the estimated wavenumber-domain reflection matrix \mathbf{C}_r reproduces the directional reflection behavior. To ensure sufficient angular resolution, a Fibonacci lattice with 2401 wavenumber bins was employed for the reconstruction. Owing to the uniform angular sampling, both specular and scattered components are smoothly visualized over the entire angular range.

These results demonstrate that the proposed method robustly and accurately estimates the wavenumber-domain reflection matrix \mathbf{C}_r for a wide variety of boundary conditions, ranging from purely specular surfaces to strongly scattering periodic structures. Furthermore, the reconstructed reflection maps confirm that directional reflection behavior can be reproduced with high fidelity using the estimated operator.

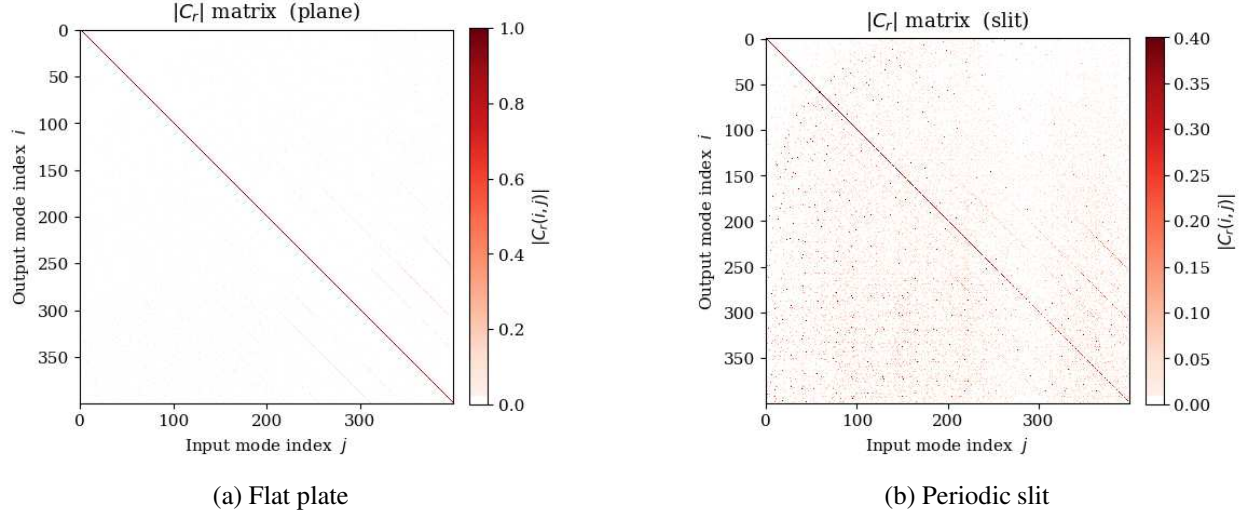


Figure 3: Estimated wavenumber-domain reflection matrices \mathbf{C}_r . For the flat plate, energy is concentrated along the main diagonal, indicating dominant specular reflection. In contrast, the periodic slit exhibits pronounced off-diagonal components, corresponding to multi-directional scattering.

5 Numerical Experiment II: Sound-Field Simulation Using the Wavenumber-Domain Acoustic Admittance

5.1 Simulation Conditions

In this section, the wavenumber-domain acoustic reflection coefficients estimated in the previous chapter are converted into their admittance representation and incorporated into the Boundary Element Method (BEM) to evaluate sound-field reproduction performance. Two BEM approaches are compared:

(i) a conventional BEM in which the flat and slit reflectors are explicitly meshed in detail, and (ii) the proposed BEM, in which only the flat surface is meshed and the wavenumber-domain admittance is imposed as a boundary condition.

The reflector surface was positioned such that its upper boundary corresponds to $z = 0$ m. A monopole source was placed at $(x, y, z) = (0$ m, 0 m, 0.4 m) to excite a steady-state field at 3400 Hz.

In the conventional BEM, discretizing the reflector geometry with a mesh size of approximately 30 mm resulted in 5,830 boundary elements for the flat plate and 15,180 elements for the slit reflector. In contrast, the proposed BEM employs only the 5,830-element flat-surface mesh, using the same mesh even for the slit condition while imposing the wavenumber-domain admittance estimated in the previous chapter.

Sound pressure was evaluated on two orthogonal cross sections ($x = 0$ and $y = 0$) over a region of 1.5 m \times 1.0 m with observation points placed at 0.05 m intervals. The speed of sound was set to $c = 343.5$ m/s.

5.2 Results

Figure 5 compares the magnitude distributions of the total acoustic field (incident + reflected) obtained using the conventional BEM and the proposed BEM for both the flat and slit boundary conditions.

For the flat-plate condition, the sound fields produced by the two methods agree almost perfectly, indi-

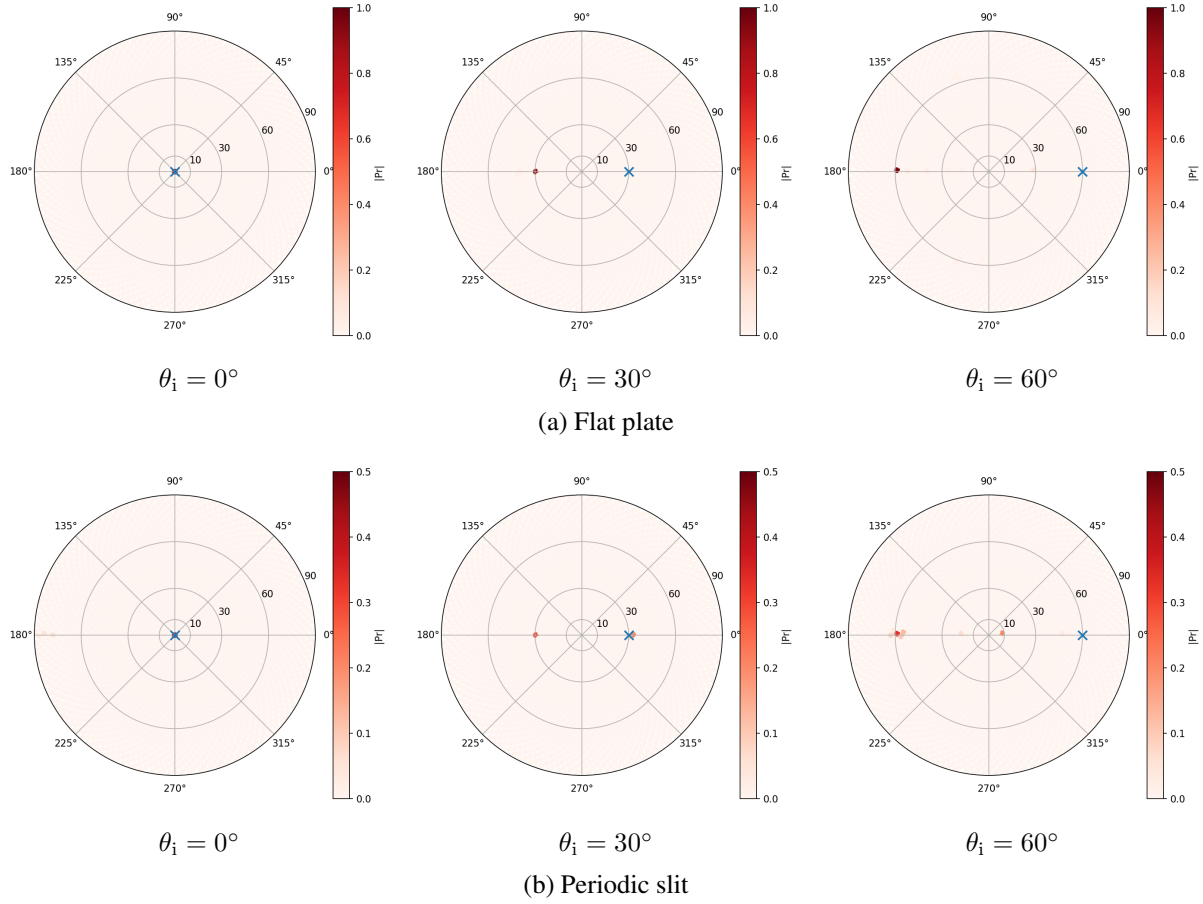


Figure 4: Reconstructed reflection directivity maps $|P_r|$ computed using the estimated C_r . Blue crosses indicate the incident directions.

cating that specular reflection is reproduced with high accuracy. Under the slit condition, a highly complex scattering field is formed due to diffraction and interference caused by the openings. The proposed BEM successfully reconstructs these features with accuracy comparable to that of the conventional BEM.

A quantitative comparison was performed by computing the cosine similarity and mean squared error (MSE) relative to the conventional BEM results. For the flat-plate case, the similarity was 0.982 with an MSE of 5.73×10^{-3} . For the slit case, the similarity was 0.981 with an MSE of 5.74×10^{-3} . Both results indicate excellent agreement.

A particularly noteworthy finding is that the proposed BEM achieves this accuracy with far fewer boundary elements. Whereas the conventional BEM required 5,830 elements for the flat plate and 15,180 elements for the slit geometry, the proposed method reproduces slit-induced diffraction and scattering using only the simple flat-surface mesh with 5,830 elements, which is identical to that used for the flat-plate case.

This demonstrates the effectiveness of externally prescribing scattering behavior through the estimated wavenumber-domain admittance, rather than explicitly meshing fine geometric details.

These results confirm that the proposed BEM based on wavenumber-domain admittance can reproduce sound fields with accuracy comparable to conventional full-geometry BEM while reducing the number of elements by more than half.

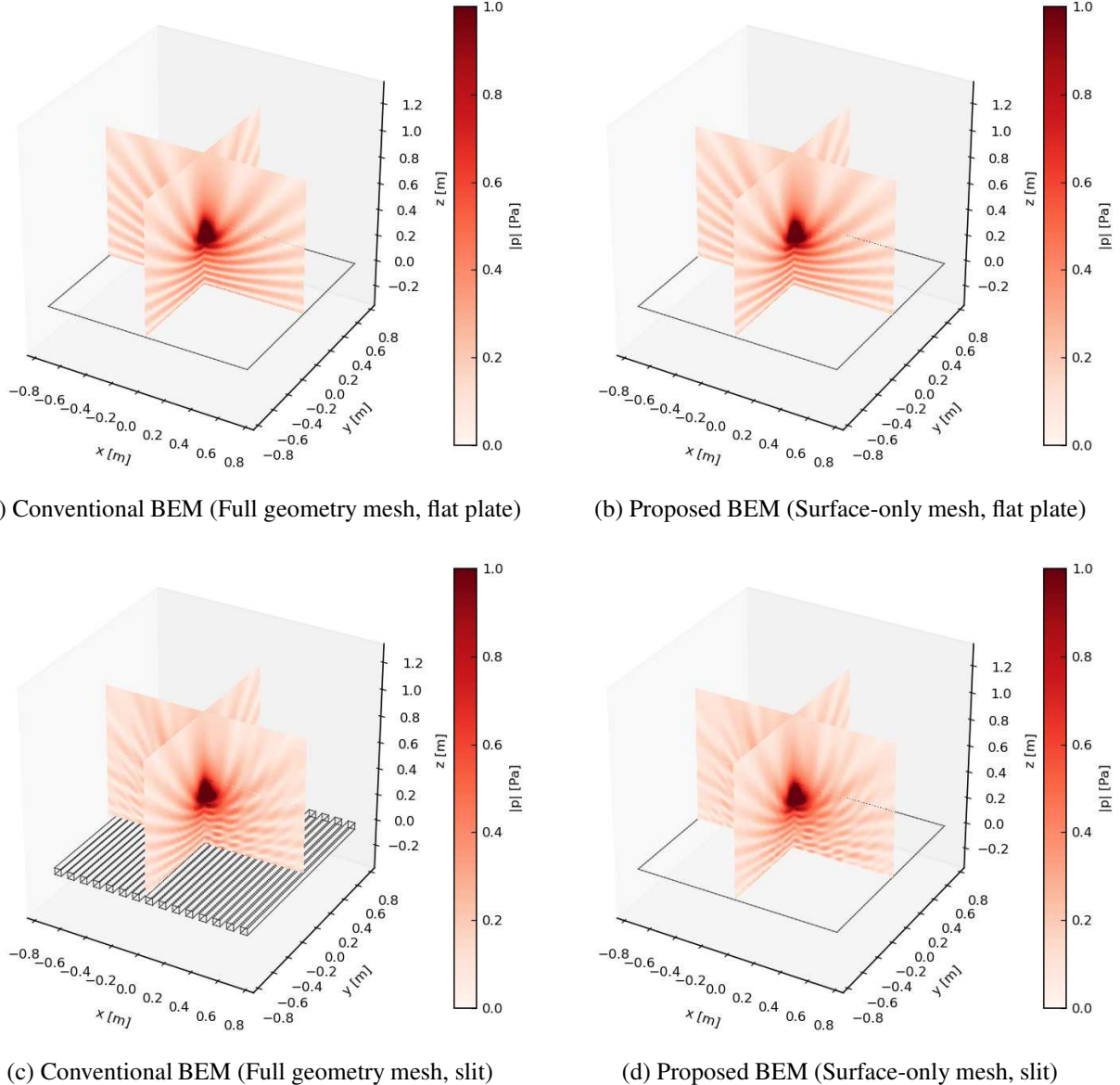


Figure 5: Comparison of total sound pressure magnitude distributions obtained by the conventional geometry-based BEM and the proposed surface-based BEM. Two boundary conditions are considered: a flat plate and a slit structure. The conventional BEM employs 5,830 boundary elements for the flat plate and 15,180 elements for the slit geometry, whereas the proposed method reproduces both cases using only the flat-surface mesh with 5,830 elements, achieving acoustic fields comparable to those predicted by the full-geometry BEM.

6 Conclusion

This study introduced a wavenumber-domain acoustic reflection coefficient C_r formulated as a linear operator that represents direction-dependent reflection and scattering behavior at an acoustic boundary. By focusing exclusively on the relationship between incident and reflected wave components at the boundary, the proposed framework provides a macroscopic description of reflection phenomena without explicitly modeling the internal structure of the material.

An estimation framework was developed in which the directional spectra of incident and reflected waves are extracted from multi-source, multi-receiver sound-pressure data via a spatial Fourier transform, and the reflection matrix \mathbf{C}_r is directly estimated from these spectra. Although sparsity-promoting solvers can be advantageous for structured or periodic boundaries, the formulation itself is independent of the specific estimation algorithm.

Once estimated, \mathbf{C}_r can be converted into a wavenumber-domain acoustic admittance and incorporated into conventional BEM formulations as a nonlocal boundary condition. This enables sound-field analysis without explicitly meshing fine geometric features, allowing complex reflection and scattering characteristics to be imposed directly at the boundary.

Three-dimensional BEM validations demonstrated that the proposed method accurately reproduces both specular reflection from a flat plate and multi-directional scattering from a periodic slit structure. The resulting sound fields showed excellent agreement with those obtained using geometry-resolved BEM, while significantly reducing modeling complexity.

Unlike conventional scalar reflection models defined independently for each incident angle, the proposed matrix-valued formulation captures both directional dependence and scattering-induced coupling in a unified framework. Future work will focus on experimental estimation for real materials and extensions to more complex acoustic boundaries.

Acknowledgments

This work was supported by JSPS KAKENHI Grant Number JP24K03222.

References

- [1] D. L. Johnson, J. Koplik, and R. Dashen, “Theory of dynamic permeability and tortuosity in fluid-saturated porous media,” *J. Fluid Mech.*, 1987.
- [2] Y. Champoux and J.-F. Allard, “Dynamic tortuosity and bulk modulus in air-saturated porous media,” *J. Appl. Phys.*, 1991.
- [3] M. A. Biot, “Theory of propagation of elastic waves in a fluid-saturated porous solid. I. Low-frequency range,” *J. Acoust. Soc. Am.*, 1956.
- [4] M. A. Biot, “Theory of propagation of elastic waves in a fluid-saturated porous solid. II. High-frequency range,” *J. Acoust. Soc. Am.*, 1956.
- [5] M. S. Kushwaha, P. Halevi, L. Dobrzynski, and B. Djafari-Rouhani, “Theory of acoustic band structure of periodic elastic composites,” *Phys. Rev. B*, 1993.
- [6] J.-P. Groby, W. Dante, and C. Depollier, “Acoustic metaporous plates for sound absorption and insulation,” *J. Acoust. Soc. Am.*, 2011.
- [7] M. Tamura, “Spatial Fourier transform method of measuring reflection coefficients at oblique incidence. I: Theory and numerical examples,” *J. Acoust. Soc. Am.*, 1990.
- [8] M. Tamura, J.-F. Allard, and D. Lafarge, “Spatial Fourier-transform method for measuring reflection coefficients at oblique incidence. II. Experimental results,” *J. Acoust. Soc. Am.*, 1995.

- [9] S. Hoshika, T. Iwami, A. Omoto, and S. Sugie, “Acoustic reflection angular spectrum estimation using multi-point impulse responses and spatial Fourier transforms,” *Acoust. Sci. Technol.*, 2025.
- [10] S. Hoshika, T. Iwami, and A. Omoto, “Numerical modeling of acoustic scattering characteristic with wavenumber domain admittance,” *INTER-NOISE 2024 Proc.*, 2024.
- [11] E. G. Williams, *Fourier Acoustics*, Academic Press, 1999.
- [12] P. M. Morse and K. U. Ingard, *Theoretical Acoustics*, Princeton Univ. Press, 1986.
- [13] J.-F. Allard and N. Atalla, *Propagation of Sound in Porous Media*, Wiley, 2009.
- [14] A. J. Burton and G. F. Miller, “The application of integral equation methods to the numerical solution of some exterior boundary-value problems,” *Proc. R. Soc. Lond. A*, 1971.
- [15] S. Kirkup, *The Boundary Element Method in Acoustics*, Whittles Publishing, 1998.
- [16] R. Tibshirani, “Regression shrinkage and selection via the lasso,” *J. R. Stat. Soc. B*, 1996.